Nanoneedle-Assembled Copper/Cobalt Sulfides on Nickel Foam as an Enhanced 3D Hierarchical Catalyst to Activate Monopersulfate for Rhodamine B Degradation

Hsing-Hua Chen[a], Young-Kwon Park[b], Eilhann Kwon[c], Yiu Fai Tsang[d], Bui Xuan Thanh[e], Ta Cong Khiem[a], Siming You[f], Chechia Hu[g,], and Kun-Yi Andrew Lin[a,*]*

[a]Department of Environmental Engineering & Innovation and Development Center of Sustainable Agriculture, National Chung Hsing University, 250 Kuo-Kuang Road, Taichung, Taiwan

[b]School of Environmental Engineering, University of Seoul, Seoul 02504, Republic of Korea

[c]Department of Environment and Energy, Sejong University, 209 Neungdong-ro, Gunja-dong, Gwangjin-gu, Seoul, Republic of Korea

[d]Department of Science and Environmental Studies, The Education University of Hong Kong, Tai Po, New Territories 999077, Hong Kong

[e]Faculty of Environment and Natural Resources, Ho Chi Minh City University of Technology, 268 Ly Thuong Kiet, District 10, Ho Chi Minh City, 700000, Viet Nam

[f]James Watt School of Engineering, University of Glasgow, Glasgow G12 8QQ, UK

[g]Department of Chemical Engineering, National Taiwan University of Science and Technology, Da'an Dist., Taipei City, Taiwan 106

*Corresponding Authors. E-mail addresses: linky@nchu.edu.tw (KYA Lin); chechia@mail.ntust.edu.tw (C. Hu).

Abstract

While metal oxides are conventionally proposed for activating monopersulfate (MPS) to degrade refractory contaminants, metal sulfides have recently gained increased attention for MPS activation because these sulfides exhibit more reactive redox characteristics to enhance the catalytic activation of MPS. The present study attempts to develop a novel material comprised of metal sulfides with 3D hierarchical nanostructures to activate MPS. Specifically, a 3D hierarchically structured catalyst was fabricated by growing CuCo-layered double hydroxide (LDH) on nickel foam (NF), followed by direct sulfurization, affording Cu/CoS@NF (CCSNF). CCSNF could exhibit a unique morphology of floral bunches comprised of nano-needles, residing on the NF surfaces. Compared with its precursor, CuCo-LDH@NF, oxide analogue, and $CuCo_2O_4$@NF, CCSNF possessed superior physical and chemical properties, including larger surface area and pore volume, higher current density, and lower charge transfer resistance. These features render CCSNF a much more effective catalyst than CuCo-LDH@NF and $CuCo_2O_4$@NF for activating MPS to degrade Rhodamine B (RB). In particular, RB degradation by CCSNF-activated MPS required an activation energy only 26.8 kJ/mol, which is much lower than the reported values. The activation mechanism and degradation pathway of RB degradation by CCSNF-activated MPS were investigated and validated through experimental evidences and density function theory calculations.

Keywords: cobalt sulfide, Oxone, Rhodamine B, copper sulfide, nickel foam, LDH

1. Introduction

Refractory organic pollutants discharged from various industries into the environment pose great risks to the ecology in view of their toxicity, carcinogenicity, and even mutagenicity. Various treatments have been proposed for eliminating these pollutants, and advanced oxidation processes (AOPs) are consistently considered as useful methods for the quick and effective elimination of contaminants from water [1, 2].

AOPs are typically associated with various reactive oxygen species (ROS), such as hydroxyl radical ($^{\bullet}OH$) and sulfate radical ($SO_4^{\bullet-}$). Although $^{\bullet}OH$-induced AOPs have been extensively employed, $SO_4^{\bullet-}$-induced AOPs have recently gained great attention for degrading refractory contaminants [3] because $SO_4^{\bullet-}$ exhibits higher oxidation power (i.e., 2.5–3.1 V), as well as a longer half-life, compared with $^{\bullet}OH$ [4].

Monopersulfate (MPS) is a favorable precursor for generating $SO_4^{\bullet-}$ because this substance is inexpensive and environmentally friendly [5]. However, MPS requires "activation" for facilitating $SO_4^{\bullet-}$ generation. MPS can be activated via several methods, among which the catalytic activation of MPS by transition metals, such as copper (Cu), cobalt (Co), and iron (Fe), is one of the most useful approaches [6-10]. Therefore, these metal ions are commonly employed for activating MPS. Unfortunately, the homogeneous characteristics of these metal ions render them challenging to recover from water [11-21].

Although metal oxides have been proposed as heterogeneous alternatives for activating MPS, metal sulfides have recently gained increased attention as heterogeneous catalysts for activating MPS because these sulfides could exhibit more reactive redox characteristics to enhance the catalytic activation of MPS [22-25]. However, studies on the use of metal sulfides for activating MPS to degrade refractory contaminants are still very limited. More importantly, because the structures of heterogeneous catalysts predominantly control their catalytic activities, catalysts with

hierarchical nanostructures are expected to exhibit larger contact surface areas and surficial reactivity for catalytic applications [26-28]. Therefore, this study attempts to develop a novel catalyst comprised of metal sulfides with 3D hierarchical nanostructures to activate MPS.

To this end, the present study proposes the construction of nanoscale metal sulfides on 3D nickel foam (NF) because NF can provide hierarchical structures to support and distribute nanoscale metal sulfides. Moreover, NF is an easy-to-use macroscale material that is easily implemented and recovered. Especially, an even more hierarchical structure is produced by adopting CuCo-layered double hydroxide (LDH) bearing a unique morphology of floral bunches comprised of nano-needles as a precursor. This CuCo-LDH is particularly grown on NF as such a CuCo-LDH can be easily transferred into Cu/Co sulfides through one-step sulfurization [29]. Such a strategy allows Cu/Co sulfides shaped as nano-needles assembled as floral bunches to be loaded on NF to form the desired 3D hierarchical macro-porous catalyst, Cu/Co sulfide@NF (CCSNF). Given its many favorable properties, CCSNF may be an advantageous heterogeneous catalyst for activating MPS to degrade refractory contaminants.

To date no such a catalyst has yet been developed for MPS activation. Thus, the present study would be the first study to investigate catalytic activities of CCSNF. CuCo-LDH@NF (CCHNF) and its oxide analogue, $CuCo_2O_4$@NF, which were derived from the calcination of CCHNF, were also tested and compared with CCSNF for MPS activation. Specifically, a carcinogenic dye, Rhodamine B (RB), was selected as a representative refractory, toxic, and widely detected contaminant [30, 31] to evaluate the MPS activation ability of these catalysts. Experimental and theoretical studies of RB degradation by CCSNF-activated MPS were then conducted to further provide insights into the behaviors and mechanisms of the catalyst for MPS activation and RB degradation.

2. Experimental

A schematic illustration of the process of CCSNF fabrication is shown in Fig. 1. NF was used as a 3D macroscale substrate for growth of CuCo-LDH. Calcination to afford the as-derived CCONF or sulfurization to afford CCSNF could then be performed. Details of the preparation, characterization, and experimental protocols of RB degradation can be found in the supporting information.

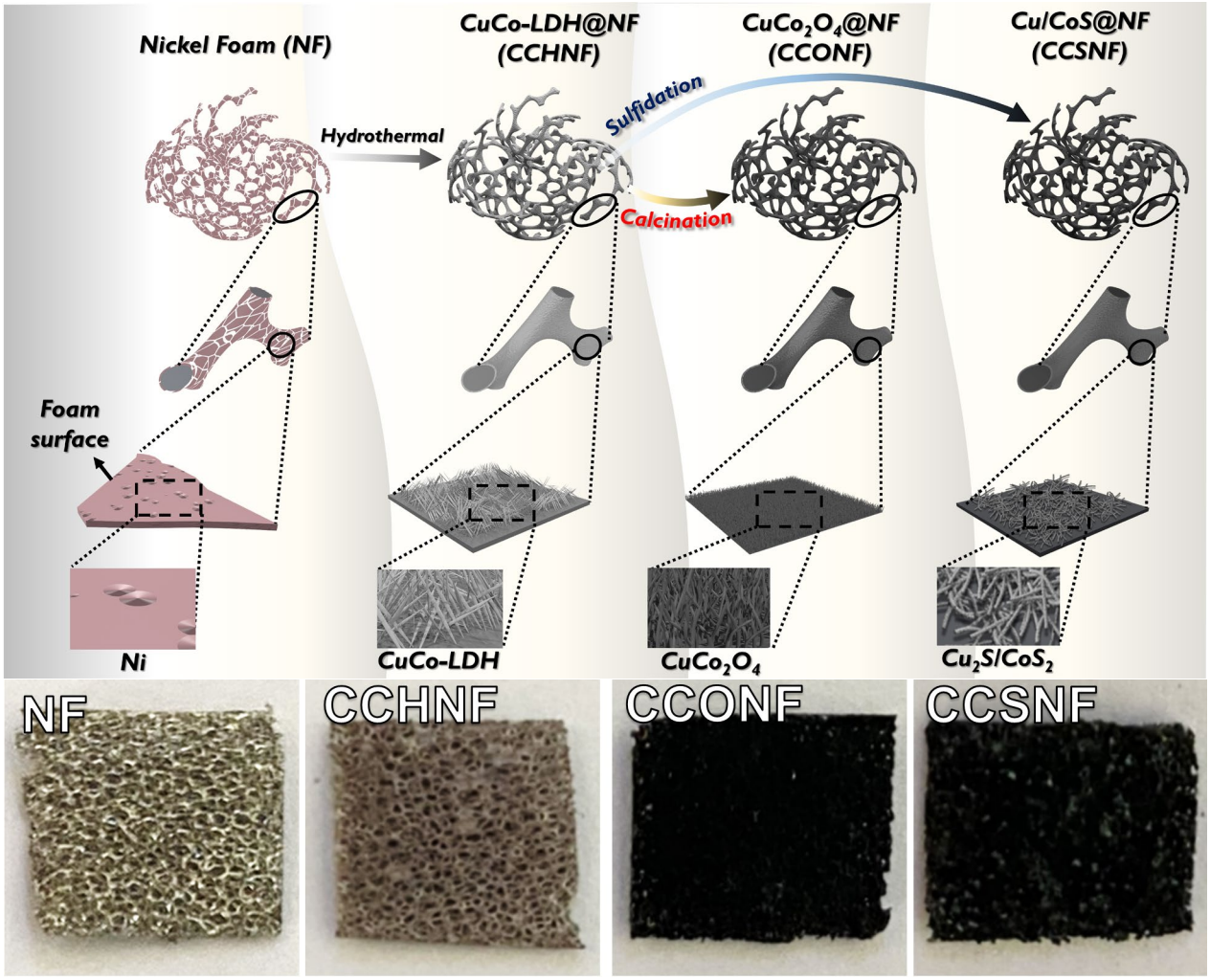

Fig. 1. Schematic illustration of the catalyst preparation process, and the corresponding photos.

3. Results and Discussion

3.1 Physical and chemical properties of CCSNF

As illustrated in Fig. 1, NF was first modified through the direct growth of CuCo-LDH to afford CCHNF. Fig. 1 displays that the original metallic color of NF changed to opaque gray, suggesting that the surface of NF had been modified. The SEM images further reveal that the relatively smooth surface of NF (Fig. 2) was covered by needle-like nanostructures, which were assembled as floral bunches. Fig. 3(a) indicates that the XRD pattern of the original NF, which included three characteristic peaks of the (111), (200), and (220) planes of Ni. Additional peaks at 11.4°, 22.7°, 33.3°, and 60.6° corresponding to the (003), (006), (012), (0.15), and (113) planes of typical LDH [32, 33] were also observed, thus verifying the formation of LDH.

As shown in Fig. 1, calcination of CCHNF in air caused the opaque gray NF to darken to black. The SEM images in Figs. 2(g-i) further reveal that the original morphology of floral-like assembly of the nano-needles was still retained. The corresponding XRD pattern of the calcined product of CCHNF exhibited strong peaks at 18.9°, 31.0°, 36.7°, 38.2°, 55.3°, 59.3°, and 65.1°, which were well-indexed to $CuCo_2O_4$ (JCPDS#01-1155). These findings confirm the transformation from CuCo-LDH to $CuCo_2O_4$.

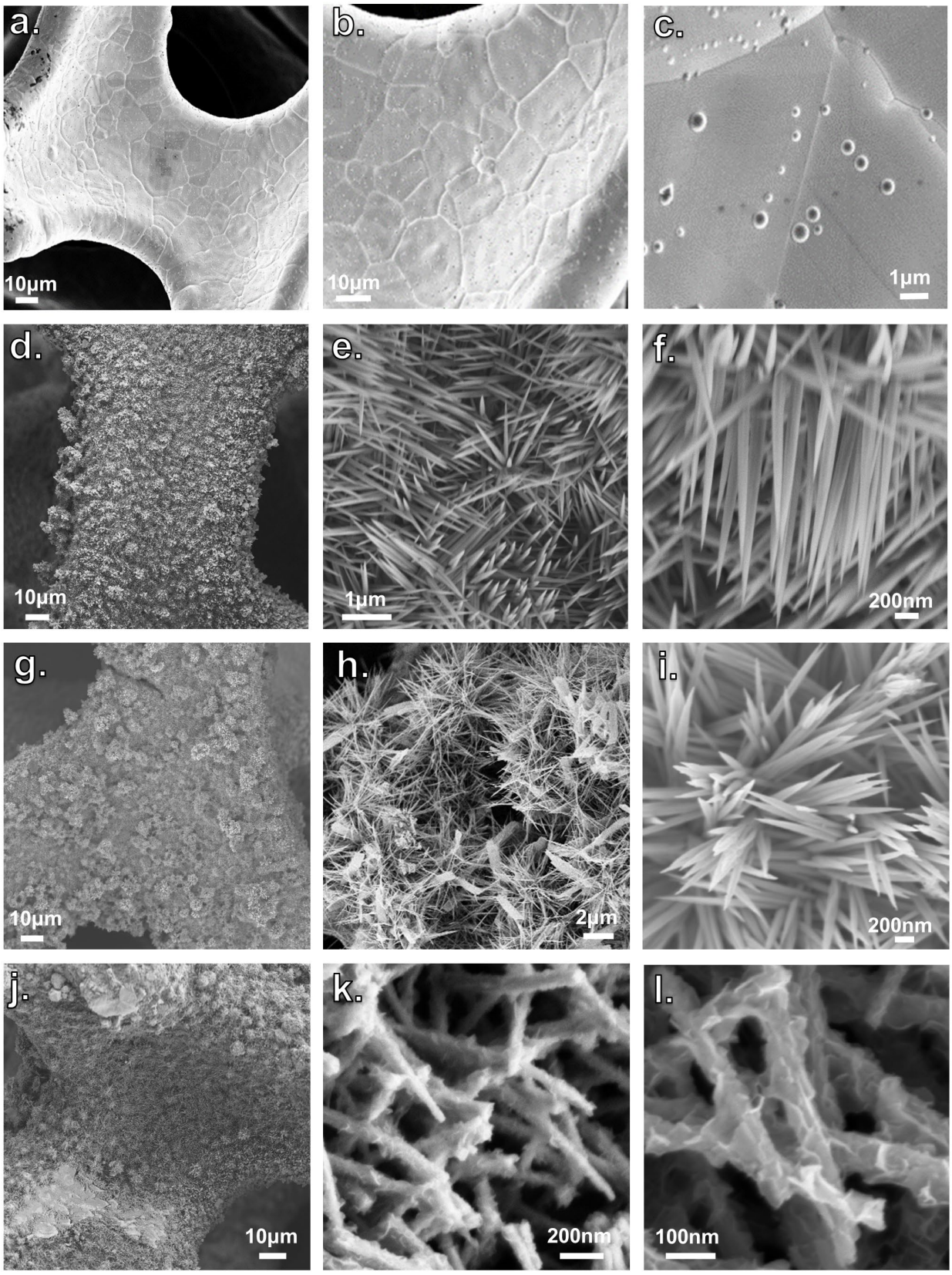

Fig. 2. SEM images of (a-c) NF, (d-f) CCHNF, (g-i) CCONF, and (j-l) CCSNF.

On the other hand, when CuCo-LDH was sulfurized, as shown in Fig. 1, the floral bunch comprised of nano-needles (Fig. 2(j)) was also perserved, and the NF surface remained completely covered by these floral bunches. However, a higher-magnification view of these bunches unveiled that the original sword-like nano-needles had become fluffy with thin films wrapping up the nano-needles. The XRD pattern of the sulfurized CuCo-LDH (Fig. 3(a)) further reveals that the disappearance of the original peaks of CuCo-LDH and the appearance of a number of peaks in the range of 20° ~ 60°; these peaks can be indexed to Cu_2S and CoS_2 and indicate the original CuCo-LDH had been successfully sulfurized to obtain Cu/Co sulfides@NF (CCSNF). Fig. 4 also validates that the signals of Cu, Co, and S were evenly distributed over NF, confirming that the NF surface was fully and uniformly covered by Cu/Co sulfides.

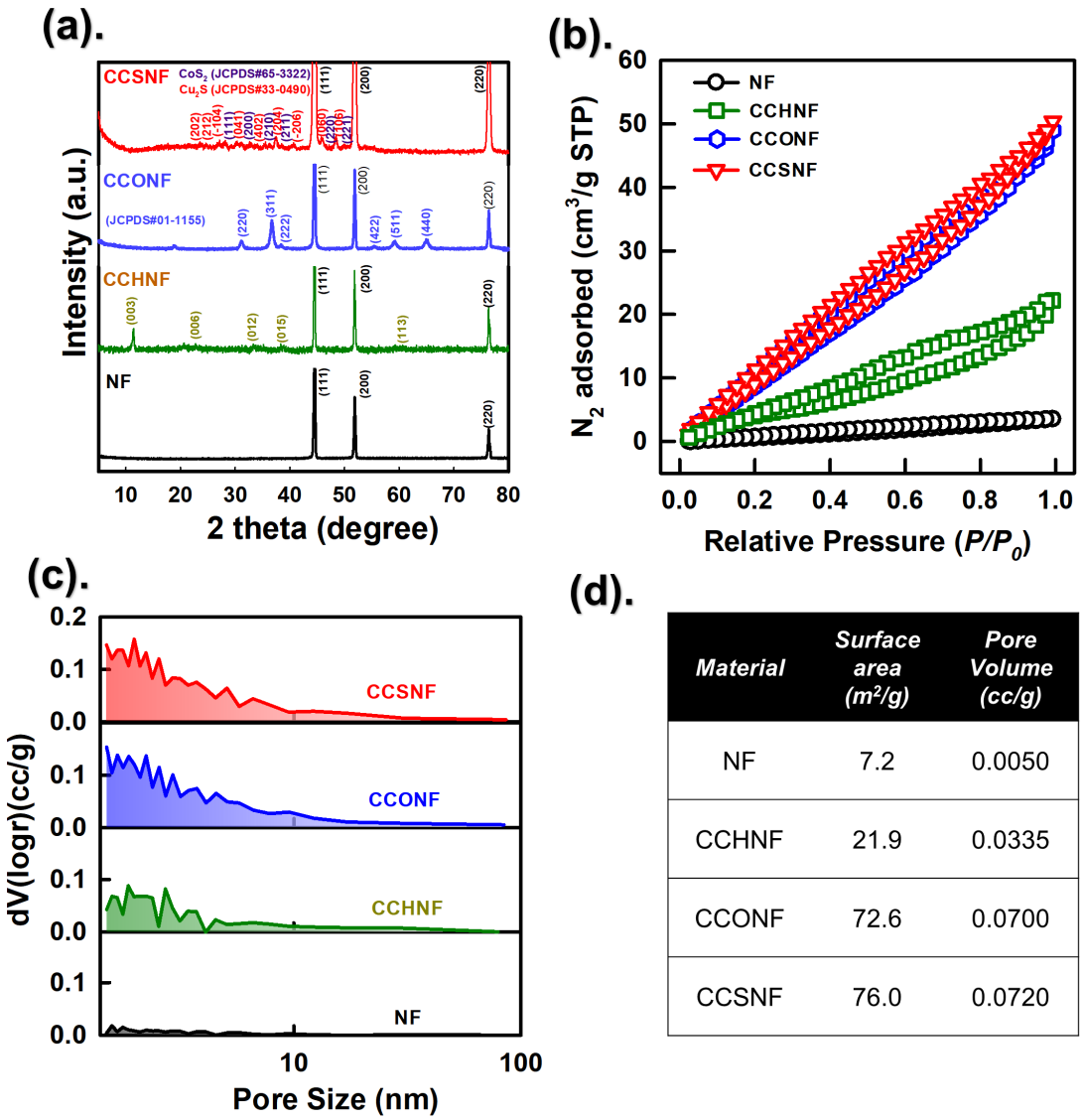

Material	*Surface area (m^2/g)*	*Pore Volume (cc/g)*
NF	7.2	0.0050
CCHNF	21.9	0.0335
CCONF	72.6	0.0700
CCSNF	76.0	0.0720

Fig. 3. (a) XRD patterns, (b) N_2 sorption isotherms, (c) pore size distributions, and (d) surface areas and pore volumes of NF, CCHNF, CCONF, and CCSNF.

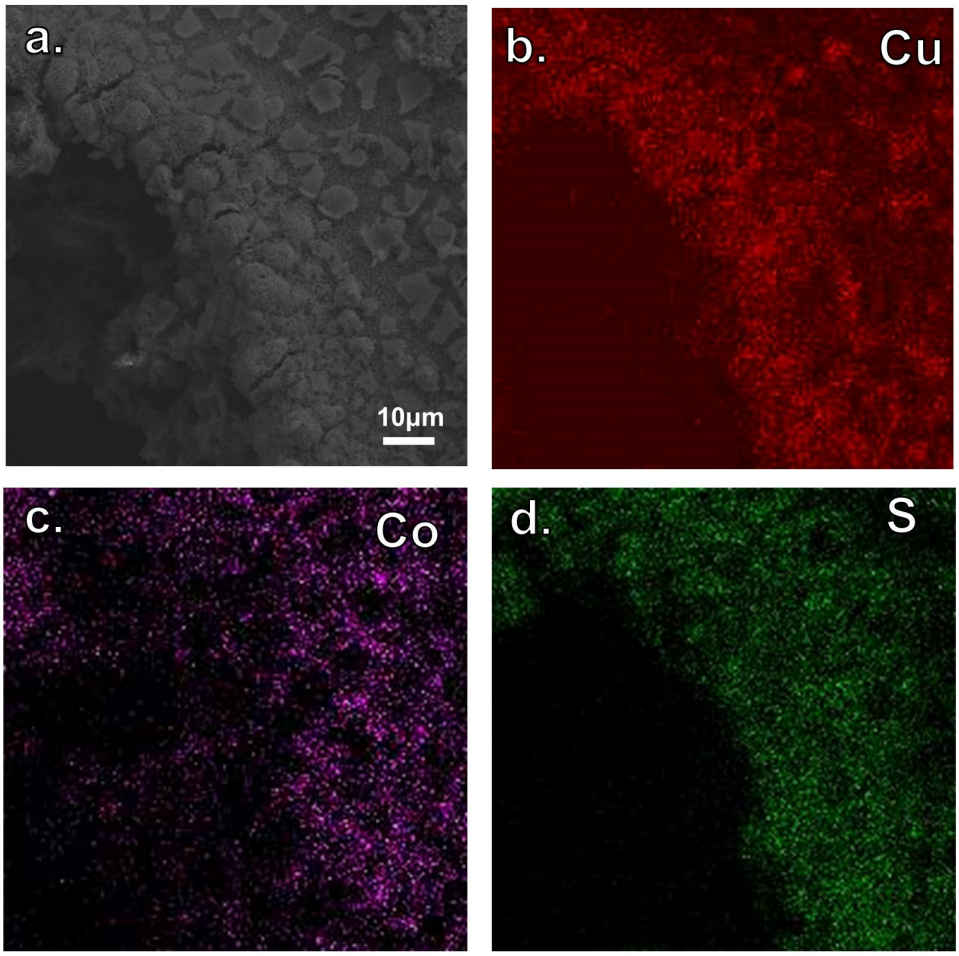

Fig. 4. Elemental mapping analysis of CCSNF: (a) Scanned region, (b) Cu, (c) Co, and (d) S.

As CCSNF exhibited a hierarchical configuration, its textural properties were analyzed by using N_2 sorption isotherms (Fig. 3(b)). For comparison, the N_2 sorption isotherms of pristine NF, CCHNF, and CCONF are shown in Fig. 3(b). The pristine material featured smooth surfaces, so its N_2 sorption amount was fairly low. The specific surface area of this material was only 7.2 m^2/g, and its pore volume was 0.0050 cc/g. When CuCo-LDH was fabricated onto NF to form CCHNF, the N_2 sorption capacity of the material noticeably increased and a hysteresis loop was observed, thus suggesting the existence of mesopores that may have been derived from the floral bunches of nano-needles. The specific surface area of CCHNF was much higher (i.e., 21.9 m^2/g) than that of the pristine material, and its total volume was 0.0335 cc/g.

Moreover, when CuCo-LDH was calcined to convert hydroxides to oxides, the corresponding N_2 sorption amount was considerably boosted, resulting in a much higher specific surface area of 72.6 m^2/g with pore volume of 0.0700 cc/g. This indicates that calcination expanded the structure of CuCo-LDH to create more micropores and mesopores as shown in Fig. 3(c). On the other hand, when CuCo-LDH was sulfurized, instead of being calcined, the resulting Cu/CoS@NF (CCSNF) also exhibited remarkable N_2 sorption capacity and the hysteresis loop could be observed, thereby indicating the presence of mesopores (Fig. 3(c)). This finding demonstrates that sulfurization could also substantially modify CuCo-LDH to endow it with a large contact surface area of 76.0 m^2/g and porous structure with a pore volume of 0.072 cc/g.

As shown in Fig. 5, the electrochemical properties of the catalysts were examined by using cyclic voltammetry (CV) and electrochemical impedance spectroscopy (EIS). Fig. 5(a) clearly indicates that CCSNF exhibited a much higher current density and reductive capability than CCONF and CCHNF. This finding suggests that the electron transfer processes between MPS and the catalysts would be more significantly enhanced in CCSNF than in CCONF and CCHNF. Furthermore, the Nyquist plot of CCSNF exhibited a much smaller arc radius compared with those of CCONF and CCHNF, thus confirming that CCSNF possessed a much lower charge transfer resistance than the latter materials. These characterizations indicate that CCSNF exhibits much more advantageous features than its precursor, CCHNF, and oxide analogue, CCONF, to activate MPS for RB degradation.

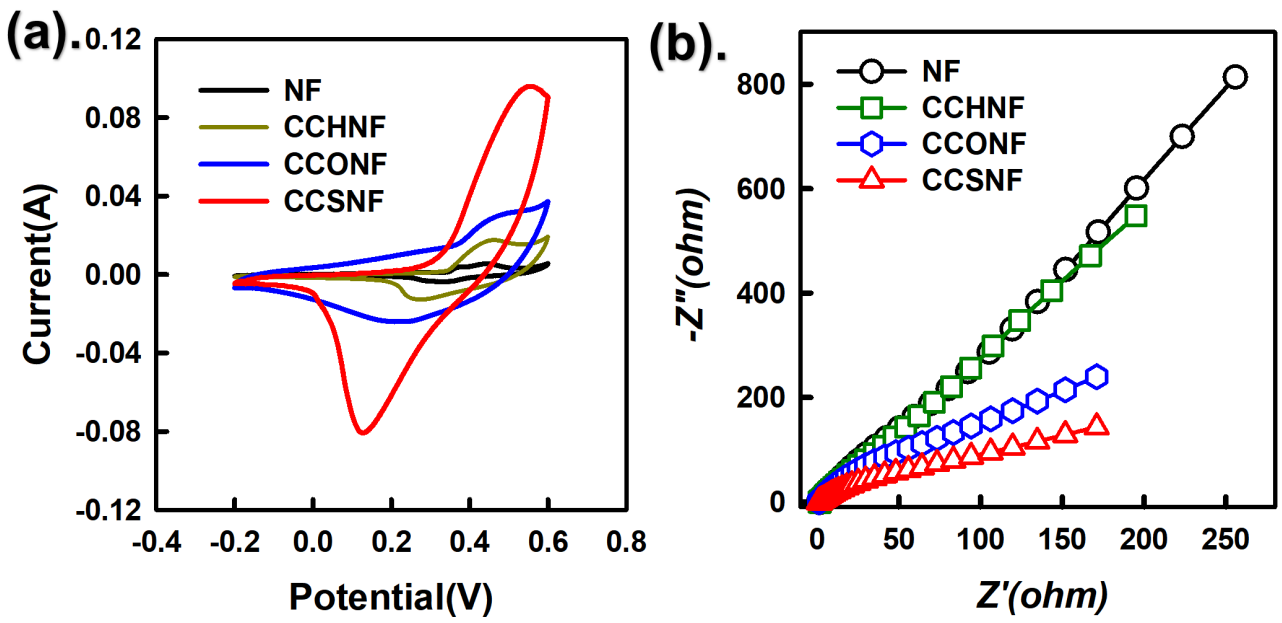

Fig. 5. (a) CV curves, and (b) EIS plots of NF, CCHNF, CCONF, and CCSNF.

The surface chemistry of CCSNF was further examined by electron spectroscopy. Fig. 6(a) shows the Cu2p spectrum of CCSNF, in which two signature peaks of Cu at 932.9 eV (i.e., $Cu2p_{1/2}$) and 952.8 eV (i.e., $Cu2p_{3/2}$). Specifically, these peaks have been correlated with Cu^{+} [34]. The Co2p spectrum displayed in Fig. 6(b) shows several noticeable peaks can be detected at 778.0 and 781.1 eV, which correspond to $Co2p_{3/2}$ and at 794.1 and 797.0 eV, which correspond to Co $2p_{1/2}$; these peaks collectively suggest the presence ofCo2+ [35]. The S2p spectrum was then analyzed (Fig. 6(c)) and two underlying peaks were found at 162.0, and 163.1 eV, corresponding to $S2p_{3/2}$ and $S2p_{3/2}$, respectively [35]. Fig. 6(d) also reveals the Ni2p spectrum of CCSNF, which exhibited a series of typical peaks derived from the modified NF. In particular, the peaks in the range of 852 - 868 eV were ascribed to the $Ni2p_{3/2}$ of NiO, whereas the peaks in the range of 870 - 884 eV were attributed to $Ni2p_{1/2}$[36].

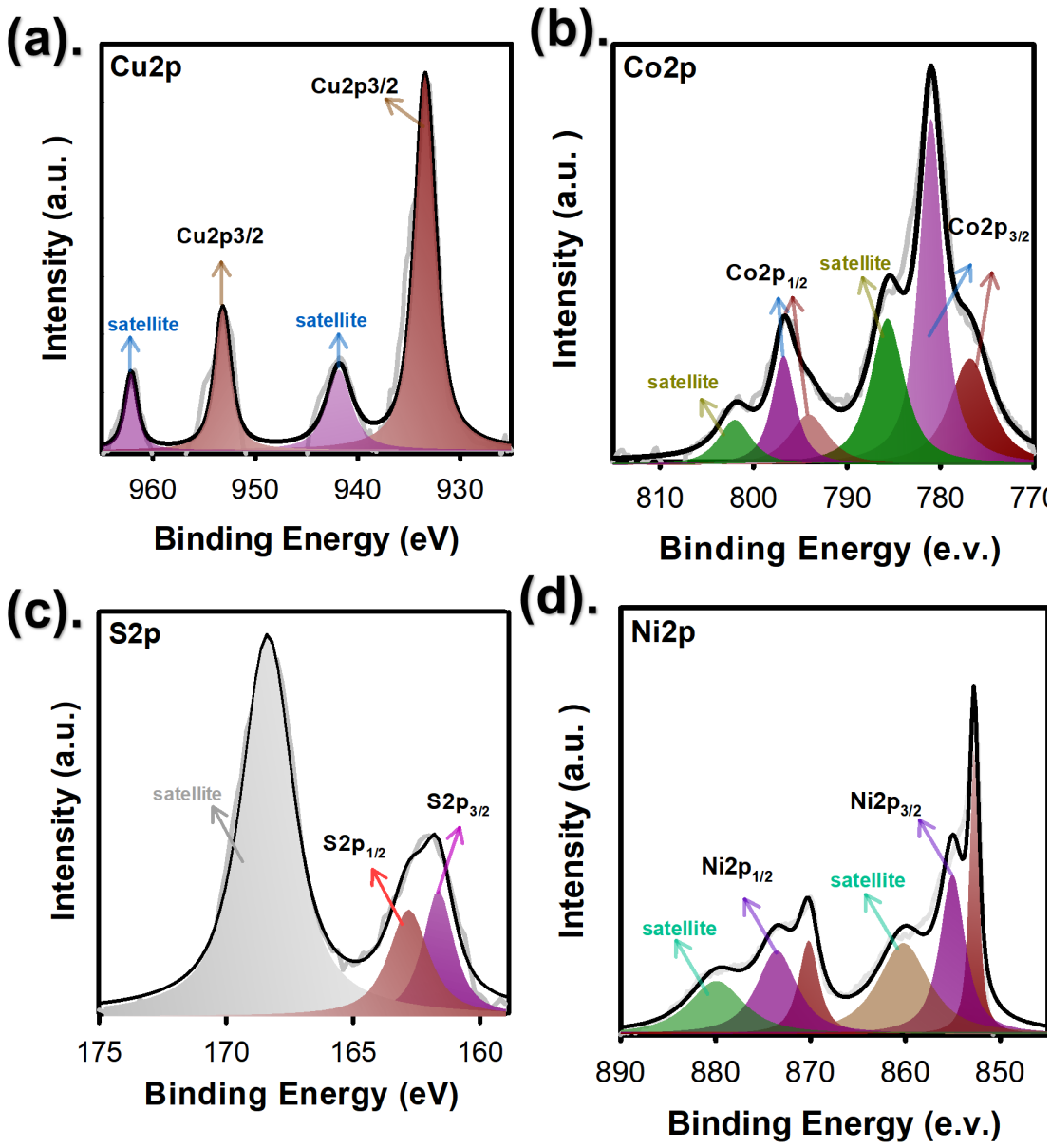

Fig. 6. XPS spectral analysis of CCSNF: (a) Cu2p, (b) Co2p, (c) S2p, and (d) Ni2p spectra.

3.2 RB degradation by MPS: Comparisons among various catalysts

Evaluation of the catalytic activities of CCSNF, CCONF, and CCHNF must begin by assessing the RB degradation capacity of MPS itself to obtain critical baseline information. Fig. 7(a) shows that addition of MPS alone to the RB solution leads to hardly any dye degradation, specifically, C_t/C_0 at 60 min was 0.98, indicating that MPS

itself without activation was incapable of degrading RB. Furthermore, addition of CCHNF resulted in rapid RB degradation and C_t/C_0 approached zero after 60 min, showing that CCHNF could activate MPS to degrade RB. When CCONF was added to MPS, RB was also quickly eliminated and completely removed after 60 min. Especially, the degradation kinetics of CCONF appeared to be much faster than that of CCHNF, indicating that CCONF possesses a comparatively higher catalytic activity for activating MPS to degrade RB. When CCSNF was added to the reaction system, RB degradation proceeded even faster and C_t/C_0 reached zero within 45 min.

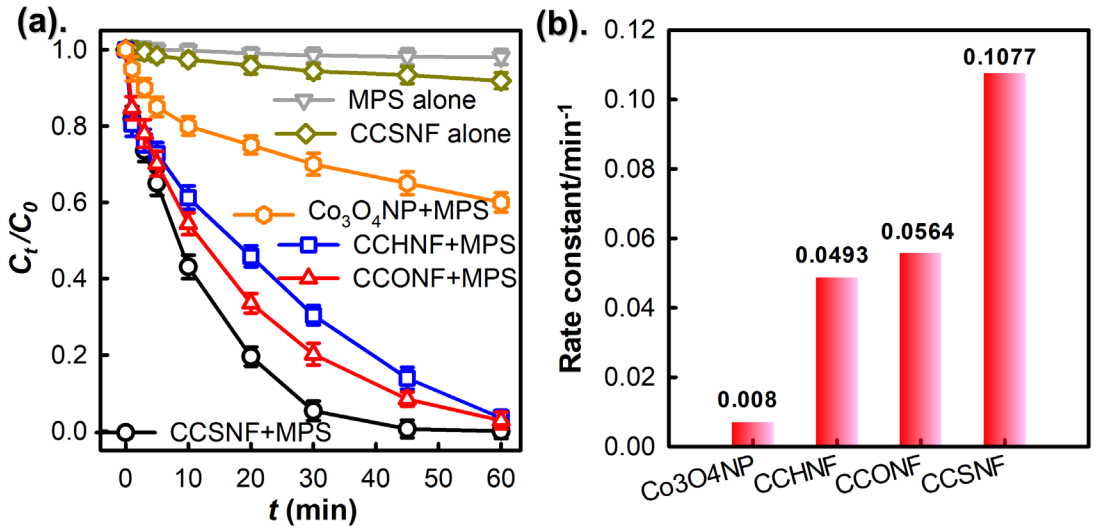

Fig. 7. (a) Degradation curves, and (b) rate constants of RB using MPS activated by various materials (Catalyst = 100 mg/L, MPS = 100 mg/L, T = 30 °C).

The degradation kinetics of the different catalysts were quantified by adopting the pseudo first-order rate law $C_t = C_0 \exp(-kt)$ [37], where k represents the pseudo first order rate constant (min^{-1}). This equation has been extensively adopted in many similar studies to calculate the rate constants of pollutant degradation. The corresponding rate constants are summarized in Fig. 7(b). The k values of RB degradation by CCHNF, CCONF, and CCSNF were 0.0493, 0.0564, and 0.1077 min^{-1}, respectively. This

comparison clearly indicates that CCSNF possessed much higher catalytic activities than either CCONF or CCHNF for activating MPS to degrade RB.

In addition to RB, three other toxic dyes, namely Acid Red 27 (AR), Methyl Orange (MO), and Methylene Blue (MB), were selected and tested to compare the catalytic activities of CCSNF, CCONF, and CCHNF for MPS activation. Figs. 8 (a) and (b) show the AR degradation profiles of the three catalysts; here, CCSNF substantially outperformed CCONF and CCHNF for activating MPS to degrade AR. Figs. 8(c) and (d) reveal the MO degradation by the three catalysts, and CCSNF exhibited a tremendously higher k compared with CCONF and CCHNF for MO degradation. Similarly, Figs. 8(e) and (f) display the MB degradation using the three catalysts, and CCSNF enabled the complete elimination of MB within 45 min, while CCONF and CCHNF could not achieve complete removal of MB even after 60 min. These results confirm that CCSNF certainly had a much higher catalytic activity than the two other catalysts.

The excellent catalytic activities of CCSNF could be attributed to a number of its advantageous features. First, compared with the other catalysts, CCSNF exhibited superior textural properties on account of its nano-needles wrapped with thin films to create more contact surfaces. Second, CCSNF possessed the higher current density and reductive capability and lower charge transfer resistance compared with CCONF and CCHNF for facilitating reactions with MPS.

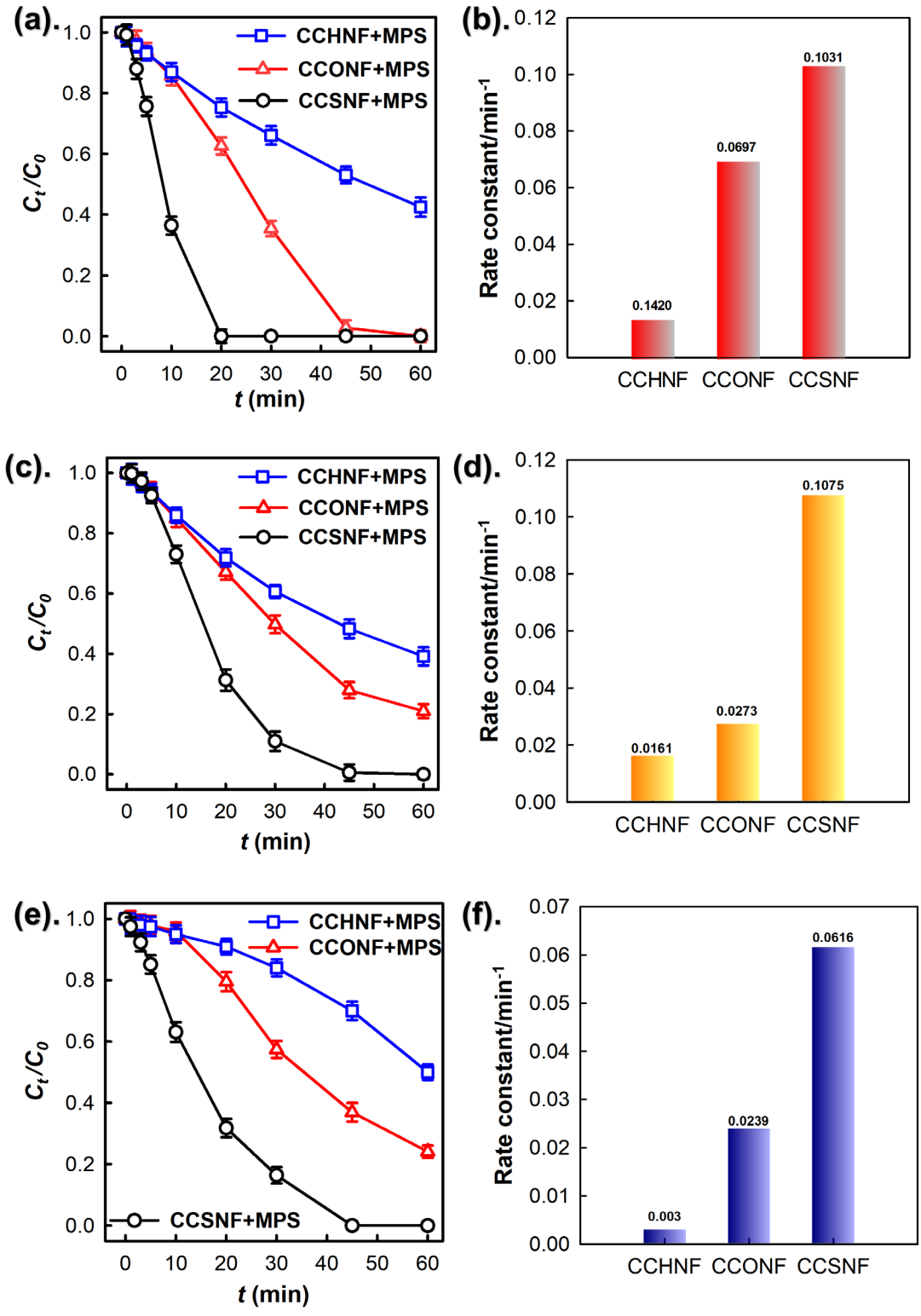

Fig. 8. Degradation curves and rate constants of (a, b) AR, (c, d) MO, and (e, f) MB using MPS activated by various materials (Catalyst = 100 mg/L, MPS = 100 mg/L, T = 30 ℃).

On the other hand, because Co_3O_4 is a benchmark heterogeneous catalyst for MPS activation, commercial Co_3O_4 nanoparticles were tested for comparison with CCSNF. Fig. 8(a) shows that Co_3O_4 could activate MPS to degrade RB, however, C_t/C_0 of RB at 60 min by Co_3O_4 was 0.6, and the corresponding k was merely 0.008 min^{-1}. These findings demonstrate that CCSNF exhibited much higher catalytic activities than the commercial Co_3O_4 nanoparticles for activating MPS and validate the superior properties of the proposed catalyst.

3.3 Effects of CCSNF and MPS concentrations on RB degradation

Further examination of the effects of the concentrations of CCSNF and MPS on RB degradation was conducted and the results are shown in Fig.9(a). The initial concentrations of CCSNF were set to 50, 75, and 100 mg/L and the MPS concentration was held constant at 100 mg/L. Complete elimination of RB was achieved within 60 min at all CCSNF concentrations tested, indicating that even a low concentration of CCSNF of 50 mg/L is capable of activating MPS to eliminate RB completely.

However, the degradation process proceeded much faster at higher CCSNF concentrations. The k values of CCSNF were 0.0486, 0.0614, and 0.1077 min^{-1} at 50, 75, and 100 mg/L, respectively (see the inset in Fig. 9(a)). These results indicate that higher concentrations of CCSNF considerably enhanced the degradation kinetics of the catalytic system as more active sites are present in the solution to speed up the reaction.

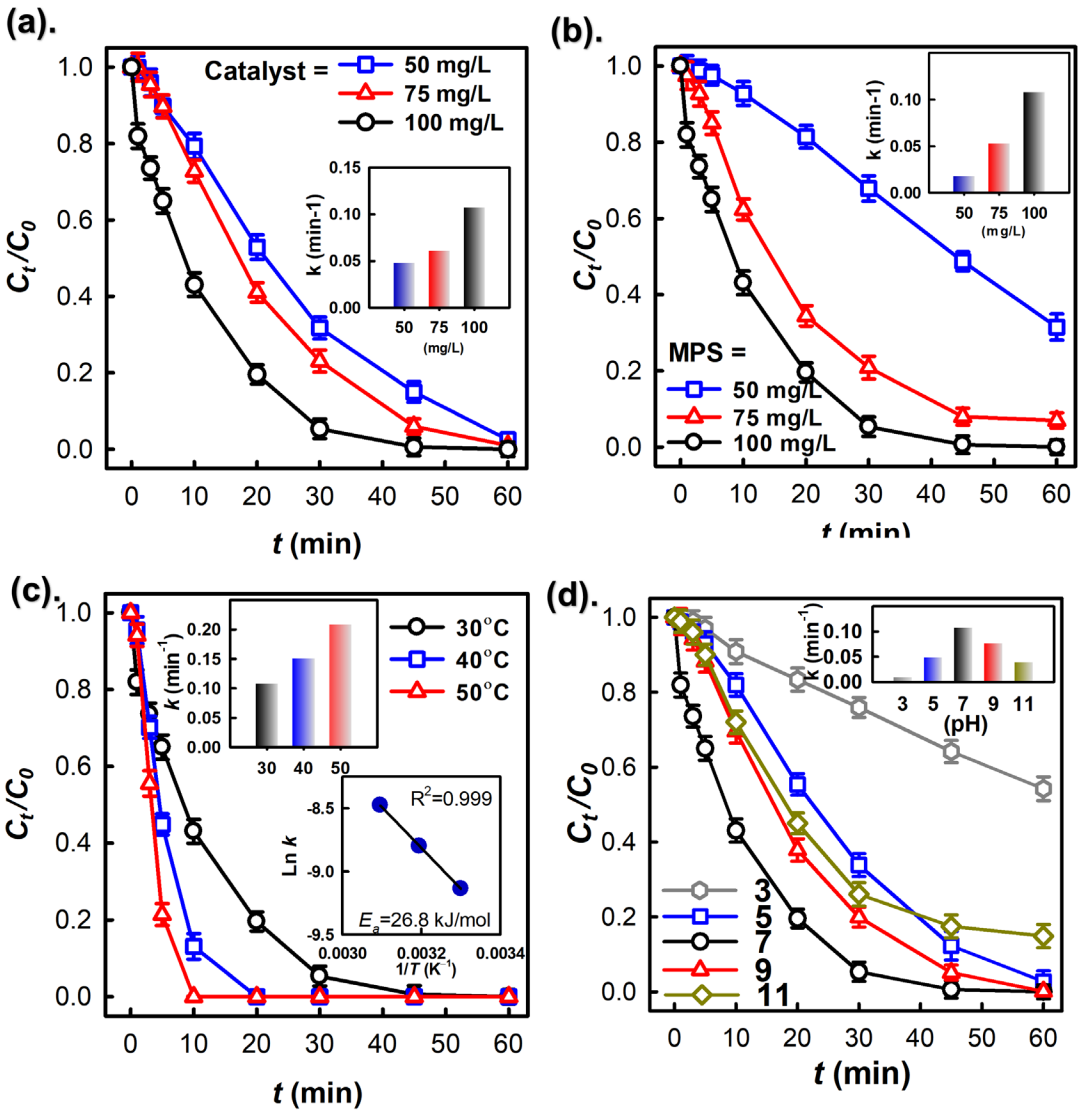

Fig. 9. Effects of (a) catalyst dosage, (b) MPS dosage, (c) temperature, and (d) pH on the degradation and rate constants of RB degradation using MPS activated by CCSNF (Catalyst = 100 mg/L, MPS = 100 mg/L, T = 30 °C).

In another set of experiments, the initial MPS concentrations were set to 50, 75, and 100 mg/L amd the concentration of CCSNF was held constant at 100 mg/L. Fig. 9(b) shows that a low concentration of MPS of 50 mg/L could lead to incomplete degradation of RB, with the *k* value of only 0.0176 min^{-1} (as shown in the inset). When the concentration of MPS increased from 50 mg/L to 75 mg/L and 100 mg/L, the degradation rate remarkably increased to 0.0530 and 0.1077 min^{-1}, respectively. These

results suggest that MPS concentration is crucial to the degradation process and that sufficient MPS is required to enable the complete elimination of RB.

3.4 Effects of temperature and pH on RB degradation

Fig. 9(c) reveals RB degradation by CCSNF-activated MPS at various temperatures. RB could be completely eliminated at temperatures ranging from 30 °C to 50 °C. RB degradation also seemed to proceed much faster at higher temperaturesthan at lower ones. The corresponding *k* increased substantially from 0.1077 at 30 °C to 0.1508 at 40 °C and 0.2084 min^{-1} at 50 °C (Fig.9(c) inset), thus validating the positive effect of elevated temperatures on the reaction.

The relationship between the reaction kinetics and temperature was further assessed using the Arrhenius equation, $\ln k = \ln A - E_a/RT$, where E_a is the activation energy (kJ/mol) of RB degradation. The plot of *1/T* versus ln *k* is illustrated in the inset in Fig. 9(c). The data were well fitted by linear regression with $R^2 = 0.999$. Moreover, the calculated E_a was 26.8 kJ/mol, which is much lower than many of the E_a values reported for RB degradation, as summarized in Table S2. These results indicate that CCSNF exhibited much higher catalytic activities compared with other reported catalysts.

Because RB degradation and MPS activation are aqueous reactions, the solution pH may be a critical parameter affecting these processes. Thus, the effect of pH on RB degradation was investigated. Fig. 9(d) shows that RB degradation was noticeably limited in a weakly basic environment at pH of 9, and the corresponding *k* dropped from 0.1077 min^{-1} at pH = 7 to 0.0769 min^{-1} at pH = 9. This adverse effect became more pronounced in a highly basic environment (i.e., pH = 11). These findings suggest that a highly basic environment is detrimental to RB degradation, likely because MPS

tends to decompose without producing $SO_4^{\bullet-}$ in basic environments [38, 39]. Therefore, insufficient $SO_4^{\bullet-}$ for RB degradation was obtained. A basic environment also tends to render the surface of CCSNF more negatively charged due to the accumulation of OH^- as revealed in the zeta potential results shown in Fig. S1. Negatively charged surfaces intensify electrostatic repulsion and restrain contact between $SO_4^{\bullet-}$ and CCSNF.

RB degradation was slightly affected by acidic environment (i.e., pH =5), and *k* decreased to very small values. Indeed, when the pHof the RB solution was set to 3, the dye was barely eliminated. This finding may be attributed to the high stability of MPS in acidic environments, which prohibits its activation [39]. These aforementioned results of RB degradation at various pH values also indicate that the optimal pH for RB degradation by CCSNF and MPS is a neutral condition (i.e., pH = 7).

3.5 Effects of textile dyeing additives and Recyclability of CCSNF

Since Rhodamine B (RB) is extensively employed in textile dyeing industries, we further simulated how RB would be degraded by CCSNF-activated MPS in effluents from textile dyeing industries. Especially, as several additives would be adopted during textile dyeing processes, such as salts containing chloride (Cl^-), bicarbonate (HCO_3^-), and nitrate (NO_3^-) ions [40, 41], the effects of these ions on RB degradation are then also investigated.

When chloride ion was present, RB degradation was slightly influenced as the rate constant changed from 0.1077 to 0.0705 min-1. This was possibly due to the fact that Cl^- would react with radicals (e.g., $SO_4^{\bullet-}$), and become chloride radicals which exhibit less oxidation power than $SO_4^{\bullet-}$, thereby leading to the slower degradation process [42]. Nevertheless, RB was still completely degraded in the presence of Cl^-.

On the other hand, RB degradation was also influenced in the presence of bicarbonate ion as the corresponding k decreased to 0.0463 min^{-1}. However, as C_t/C_0 at 60 min was 0.05, RB could be still effectively degraded using CCSNF-activated MPS. Besides, when nitrate ion was present in the RB solution, RB degradation was also noticeably affected as its corresponding k became 0.0386 min^{-1} with C_t/C_0 at 60 min = 0.08. These results indicate that > 90% of RB would be still eliminated by CCSNF-activated MPS when typical additives in textile dyeing effluents were present.

Additionally, reusability is an important consideration in the practical applications of a catalyst. In this work, the recyclability of CCSNF was investigated. Fig. 10(a) reveals the RB degradation profiles of CCSNF reused for five cycles. The profiles clearly show that RB was quickly and completely eliminated in each cycle. This finding indicates that spent CCSNF remains catalytically active and it can be reusable. Fig. 10(b) illustrates the XRD pattern of the spent CCSNF, which was comparable to that of the pristine CCSNF. On the other hand, the stability of CCSNF was additionally examined by determining metal concentrations (Cu, Co, and Ni) in RB solutions during the recyclability test using inductively coupled plasma mass spectrometry as listed in Table S2. After the 5 cycles of RB degradation, the concentrations of these metals in the solution were almost negligible (Cu: not detected, Co: 0.01 mg/L, and Ni: 0.02 mg/L) in comparison to the catalyst dosage added (i.e., 100 mg/L). These results confirm that CCSNF is a reusable and durable heterogeneous catalyst for activating MPS to degrade RB. These results confirm that CCSNF is a reusable and durable heterogeneous catalyst for activating MPS to degrade RB.

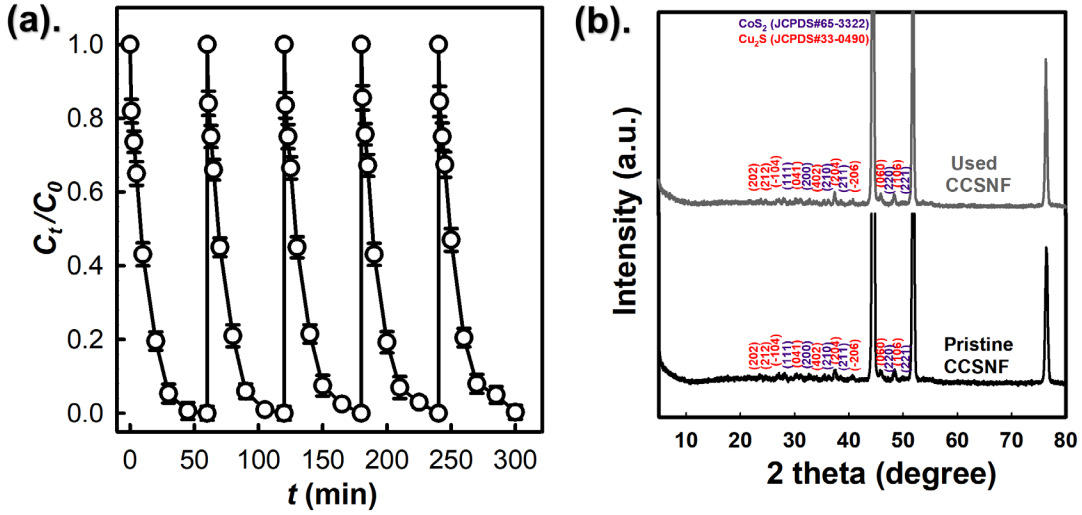

Fig. 10. (a) Recyclability of CCSNF for RB degradation (Catalyst =100 mg/L; MPS =100 mg/L; T = 30 ℃), (b) XRD pattern of the spent CCSNF.

3.6 Proposed mechanism of RB degradation by CCSNF-activated MPS

The degradation mechanism of CCSNF for activating MPS was investigated. In general, activation of MPS produces $SO_4^{\bullet-}$, which could then be transformed into other ROS. Specifically, $SO_4^{\bullet-}$ reacts with H_2O to generate hydroxyl radicals, $^{\bullet}OH$, via the reaction of $SO_4^{\bullet-} + H_2O \rightarrow SO_4^{2-} + {}^{\bullet}OH + H^+$ [43]. Therefore, $^{\bullet}OH$ may contribute to RB degradation. Superoxide ($^{\bullet}O_2^-$) and non-radical-type ROS, $^1O_2$, could also be derived from MPS for degrading organic contaminants [44-46]. Therefore, it was crucial to examine degradation mechanism of RB by CCSNF-activated MPS. To this end, the effects of scavengers on the degradation reaction were examined by using various reagents, namely, *tert*-butyl alcohol (BuOH), methanol (MeOH), benzoquinone (BQ), and NaN_3, to determine their scavenging effects on $^{\bullet}OH$, $SO_4^{\bullet-}$, $^{\bullet}O_2^-$, and $^1O_2$, respectively.

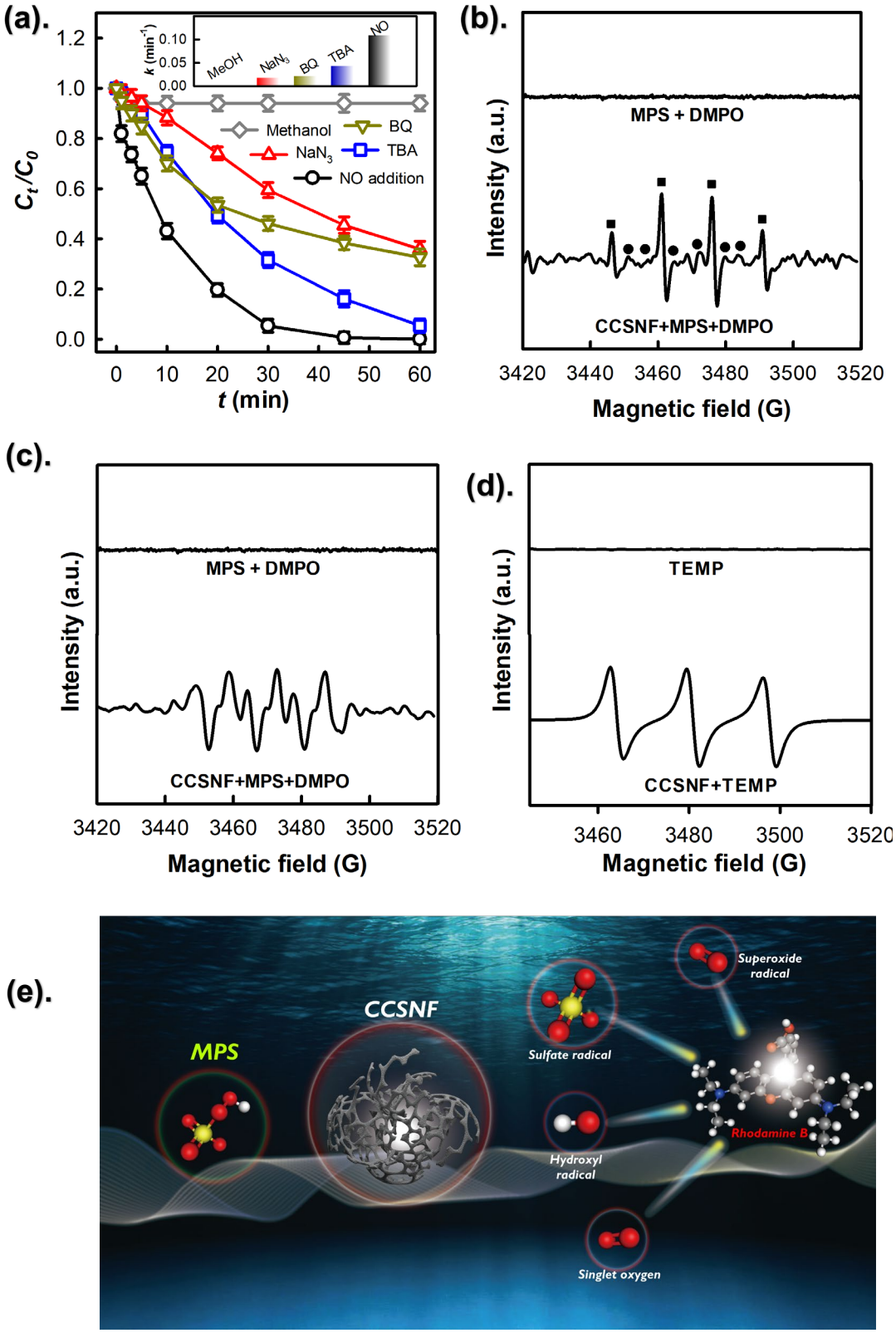

Fig. 11. (a) Effects of scavengers on RB degradation using MPS activated by various materials (Catalyst = 100 mg/L, MPS = 100 mg/L, T = 30 °C); EPR analyses using (b) DMPO, (c) DMPO in MeOH, (d) TEMP; (e) Potential mechanism of RB degradation by CCSNF-activated MPS.

Firstly, when BuOH was adopted, RB degradation was modestly affected as k decreased from 0.1077 to 0.0431 min^{-1} (the inset in Fig. 11(a)), suggesting that $^{\bullet}OH$ might exist, but $^{\bullet}OH$ seemed not the principle ROS for RB degradation. On the other hand, once MeOH was employed as the scavenger, RB degradation was almost completely inhibited (k was 0.0013 min^{-1}), signifying that $SO_4^{\bullet-}$ also existed and played an important role for RB degradation. Next, when BQ, and NaN_3 were added, RB degradation was considerably influenced, and their corresponding k values both became much lower to 0.0208, and 0.0174 min^{-1}, respectively. This implied that both $^{\bullet}O_2^-$ and $^1O_2$ also existed, derived from CCSNF-activated MPS, and participated in the RB degradation.

To further elucidate ROS derived from CCSNF+MPS, electron spin resonance analysis was then adopted in Fig. 11(b-d). At first, when 5,5-Dimethyl-1-Pyrroline-N-Oxide (DMPO) was used as a spin-trapping agent, there was no significant signal in the case of MPS itself. Nevertheless, once MPS and CCSNF were both present, a noticeable pattern could be detected, attributed to the hyperfine splitting of oxidation adduct products of DMPO-SO_4, and DMPO-OH [47-49]. Additionally, the mixture of DMPO, MPS, and CCSNF in methanol also revealed the pattern of sextet signal, which could be attributed to the presence of $^{\bullet}O_2^-$ radical [50, 51], suggesting that $^{\bullet}O_2^-$ was also present and contributing to RB degradation using CCSNF-activated MPS. On the other hand, once 2,2,6,6-Tetramethylpiperidine (TEMP) was then adopted as a spin-trapping agent in Fig. 11(d), and a distinct pattern of the triplet signal was obtained, ascribed to 2,2,6,6-Tetramethylpiperidinyloxy (TEMPO), confirming the occurrence of $^1O_2$ [52]. These results also validated that RB degradation by CCSNF-activated MPS could be attributed to a number of ROS, such as SR, $^{\bullet}OH$, $^{\bullet}O_2^-$ and $^1O_2$ as illustrated schematically in Fig. 11(e).

3.7 DFT calculation, and a potential degradation route for RB

To examine the potential degradation pathway of RB by CCSNF-activated MPS, density functional theory (DFT) calculation was employed for looking into attack of ROS on RB. The optimized structure of RB using DFT is then shown in Fig. 12(a) with its HOMO, and LUMO orbitals displayed in Fig. 12(c). As the green, and red regions represent electron-poor, and electron-rich regions of RB, the HOMO located on the benzene ring would release electrons. Thus RB would be degraded by electrophilic ROS. Fig. 7(b) summarizes Fukui indices of various reaction sites of RB. In general, a site with a higher value of Fukui indices for electrophilic attack (Fukui(-)) indicates that this specific site would undergo electrophilic attack more easily. As the site of "C6" exhibits the highest value of Fukui(-) index than any other sites, it was the most possible site of receiving radical attack. Thus, RB degradation would be possibly induced by the breakage of the bond between benzoic acid and xanthene. Additionally, the electrostatic potential distribution of RB (Fig. 12(d)) also indicates the region around "C6" would attract the anionic ROS, leading to the breakage of bonds.

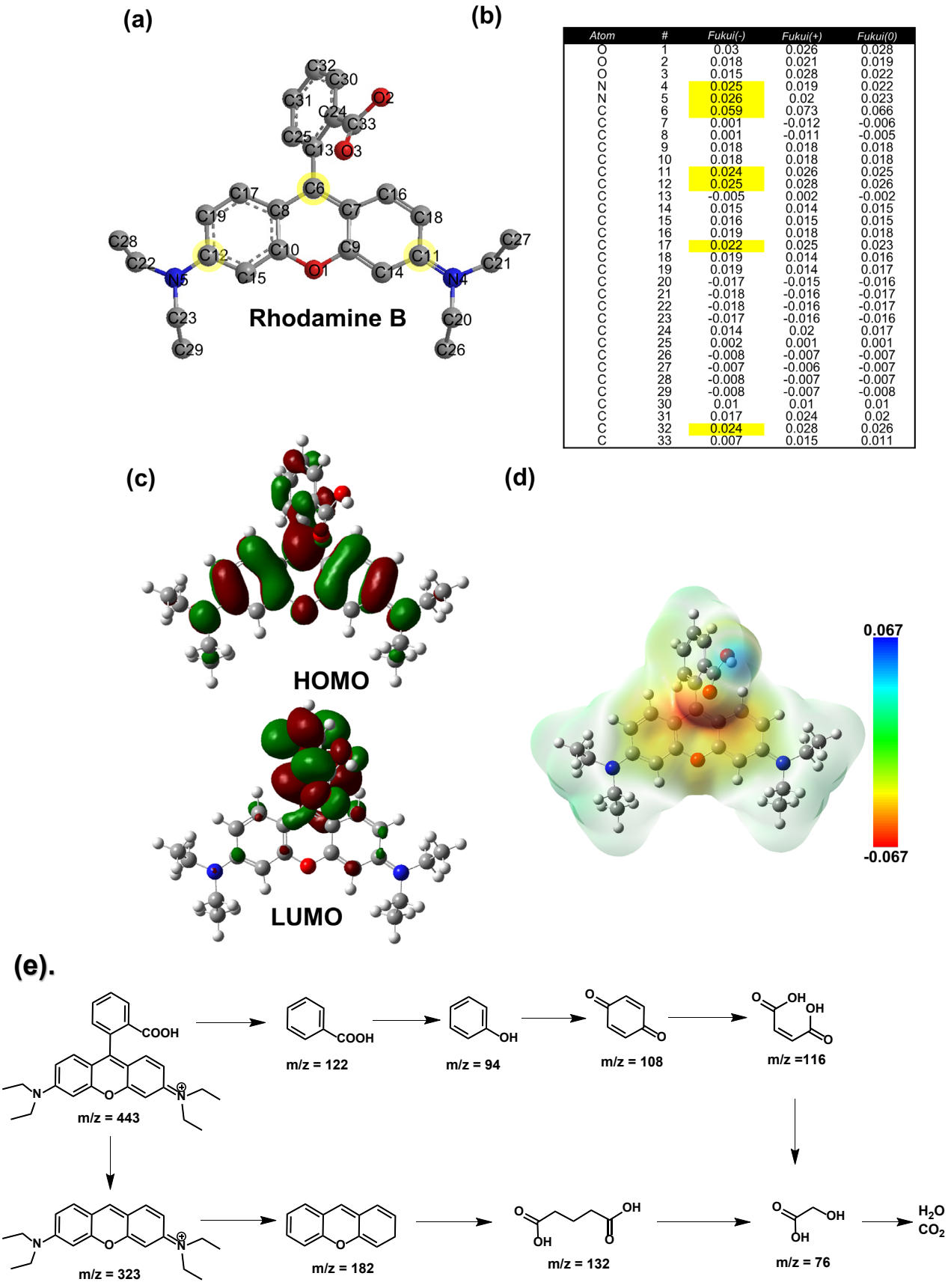

Atom	#	Fukui(-)	Fukui(+)	Fukui(0)
O	1	0.03	0.026	0.028
O	2	0.018	0.021	0.019
O	3	0.015	0.028	0.022
N	4	0.025	0.019	0.022
N	5	0.026	0.02	0.023
C	6	0.059	0.073	0.066
C	7	0.001	-0.012	-0.006
C	8	0.001	-0.011	-0.005
C	9	0.018	0.018	0.018
C	10	0.018	0.018	0.018
C	11	0.024	0.026	0.025
C	12	0.025	0.028	0.026
C	13	-0.005	0.002	-0.002
C	14	0.015	0.014	0.015
C	15	0.016	0.015	0.015
C	16	0.019	0.018	0.018
C	17	0.022	0.025	0.023
C	18	0.019	0.014	0.016
C	19	0.019	0.014	0.017
C	20	-0.017	-0.015	-0.016
C	21	-0.018	-0.016	-0.017
C	22	-0.018	-0.016	-0.017
C	23	-0.017	-0.016	-0.016
C	24	0.014	0.02	0.017
C	25	0.002	0.001	0.001
C	26	-0.008	-0.007	-0.007
C	27	-0.007	-0.006	-0.007
C	28	-0.008	-0.007	-0.007
C	29	-0.008	-0.007	-0.008
C	30	0.01	0.01	0.01
C	31	0.017	0.024	0.02
C	32	0.024	0.028	0.026
C	33	0.007	0.015	0.011

Fig. 12. Natural bond orbital (NBO) analysis for RB: (a) RB molecule structure; (b) condensed Fukui indices; (c) HOMO and LUMO of RB; and (d) Electrostatic potential (ESP)-mapped molecular surface of RB; (e) a potential degradation pathway of RB degradation by CCSNF-activated MPS.

To further identify the degradation pathway of RB by CCSNF-activated MPS, degradation intermediates were then investigated using mass spectrometry, and summarized in Table S2. According to these intermediates, a possible pathway of RB degradation was proposed as Fig. 12(e). As mentioned earlier, degradation of RB would be induced by the breakage of the bond between the benzoic acid group, and the xanthene-containing component to generate two intermediates C1, and C2. The resulting C1 (i.e., benzoic acid) would be then degraded to become C3 (phenol), and subsequently C4 (benzoquinone), which might be further attacked to produce C5, and eventually to CO_2, and H_2O. On other hand, C2 might be further decomposed to afford C6 (xanthene), then undergo ring-opening reactions to become C7 (glutaric acid), and eventually to CO_2, and H_2O.

4. Conclusions

In this study, a unique 3D hierarchically-structured catalyst was fabricated by growing CuCo-LDH on NF, followed by direct sulfurization, affording Cu/CoS@NF (CCSNF). Especially, CCSNF could exhibit a special morphology of floral bunches comprised of nano-needles, residing on the NF surfaces. In comparison to its precursor CCHNF, and oxide analogue, CCOSNF, CCSNF possessed much more superior physical and chemical properties, including higher surface area, pore volume, current density, and lower charge transfer resistance. These features made CCSNF a much more effective catalyst then CCHNF and CCONF for activating MPS to degrade the toxic contaminants, such as RB, AR, MO, and MB. In particular, RB degradation by CCSNF-activated MPS also led to the significantly lower E_a of 26.8 kJ/mol than the reported values. The activation mechanism as well as degradation pathway of RB degradation by CCSNF-activated MPS was investigated and validated through experimental evidences and DFT calculation to offer valuable insights into degradation behaviors for

developing $SO_4^{\bullet-}$-based processes of RB degradation using such a 3D hierarchical Cu/CoS-containing catalyst.

Acknowledgement:

The authors are grateful for the technical supports from National Center for High-performance Computing, Taiwan.

References:

[1] J.A. Khan, M. Sayed, S. Khan, N.S. Shah, D.D. Dionysiou, G. Boczkaj, Chapter 9 - Advanced oxidation processes for the treatment of contaminants of emerging concern, in: A.J. Hernández-Maldonado, L. Blaney (Eds.) Contaminants of Emerging Concern in Water and Wastewater, Butterworth-Heinemann, 2020, pp. 299-365.

[2] J. He, Y. Zhang, X. Zhang, Y. Huang, Highly efficient Fenton and enzyme-mimetic activities of NH2-MIL-88B(Fe) metal organic framework for methylene blue degradation, Scientific Reports, 8 (2018) 5159.

[3] S.A. Fast, V.G. Gude, D.D. Truax, J. Martin, B.S. Magbanua, A Critical Evaluation of Advanced Oxidation Processes for Emerging Contaminants Removal, Environmental Processes, 4 (2017) 283-302.

[4] T. Olmez-Hanci, I. Arslan-Alaton, Comparison of sulfate and hydroxyl radical based advanced oxidation of phenol, Chemical Engineering Journal, 224 (2013) 10-16.

[5] P. Hu, M. Long, Cobalt-catalyzed sulfate radical-based advanced oxidation: A review on heterogeneous catalysts and applications, Applied Catalysis B: Environmental, 181 (2016) 103-117.

[6] G.P. Anipsitakis, E. Stathatos, D.D. Dionysiou, Heterogeneous Activation of Oxone Using Co3O4, The Journal of Physical Chemistry B, 109 (2005) 13052-13055.

[7] G. Wei, X. Liang, Z. He, Y. Liao, Z. Xie, P. Liu, S. Ji, H. He, D. Li, J. Zhang, Heterogeneous activation of Oxone by substituted magnetites Fe3−xMxO4 (Cr, Mn, Co, Ni) for degradation of Acid Orange II at neutral pH, Journal of Molecular Catalysis A: Chemical, 398 (2015) 86-94.

[8] Z. Li, Z. Chen, Y. Xiang, L. Ling, J. Fang, C. Shang, D.D. Dionysiou, Bromate formation in bromide-containing water through the cobalt-mediated activation of peroxymonosulfate, Water Research, 83 (2015) 132-140.

[9] J. Pan, B. Gao, P. Duan, K. Guo, M. Akram, X. Xu, Q. Yue, Y. Gao, Improving peroxymonosulfate activation by copper ion-saturated adsorbent-based single atom catalysts for the degradation of organic contaminants: electron-transfer mechanism and the key role of Cu single atoms, Journal of Materials Chemistry A, 9 (2021) 11604-11613.

[10] K. Zhang, X. Min, T. Zhang, M. Si, W. Chen, Q. Wang, Y. Shi, L. Chai, Efficient peroxymonosulfate activation in electron-rich/poor reaction sites induced by copper–iron oxide heterojunctions/interfaces: Performance and mechanism, Chemical Engineering Journal, 423 (2021) 129971.

[11] Q. Yang, H. Choi, S.R. Al-Abed, D.D. Dionysiou, Iron–cobalt mixed oxide nanocatalysts: Heterogeneous peroxymonosulfate activation, cobalt leaching, and ferromagnetic properties for environmental applications, Applied Catalysis B: Environmental, 88 (2009) 462-469.

[12] C. Cai, H. Zhang, X. Zhong, L. Hou, Ultrasound enhanced heterogeneous activation of peroxymonosulfate by a bimetallic Fe–Co/SBA-15 catalyst for the degradation of Orange II in water, Journal of Hazardous Materials, 283 (2015) 70-79.

[13] H.-K. Lai, Y.-Z. Chou, M.-H. Lee, K.-Y.A. Lin, Coordination polymer-derived cobalt nanoparticle-embedded carbon nanocomposite as a magnetic multi-functional catalyst for energy generation and biomass conversion, Chemical Engineering Journal, 332 (2018) 717-726.

[14] M.-C. Li, S. Tong, J.-T. Lin, K.-Y.A. Lin, Y.-F. Lin, Electrospun Co_3O_4 nanofiber as an efficient heterogeneous catalyst for activating peroxymonosulfate in water, Journal of the Taiwan Institute of Chemical Engineers, 106 (2020) 110-117.

[15] K.-Y.A. Lin, H.-A. Chang, R.-C. Chen, MOF-derived magnetic carbonaceous nanocomposite as a heterogeneous catalyst to activate oxone for decolorization of Rhodamine B in water, Chemosphere, 130 (2015) 66-72.

[16] K.-Y.A. Lin, S.-Y. Chen, Catalytic Reduction of Bromate Using ZIF-Derived Nanoscale Cobalt/Carbon Cages in the Presence of Sodium Borohydride, ACS Sustainable Chemistry & Engineering, 3 (2015) 3096-3103.

[17] K.-Y.A. Lin, J.-T. Lin, X.-Y. Lu, C. Hung, Y.-F. Lin, Electrospun magnetic cobalt-embedded carbon nanofiber as a heterogeneous catalyst for activation of oxone for degradation of Amaranth dye, Journal of Colloid and Interface Science, 505 (2017) 728-735.

[18] K.-Y.A. Lin, T.-Y. Lin, Degradation of Acid Azo Dyes Using Oxone Activated by Cobalt Titanate Perovskite, Water, Air, & Soil Pollution, 229:10 (2018).

[19] K.-Y.A. Lin, M.-T. Yang, J.-T. Lin, Y. Du, Cobalt ferrite nanoparticles supported on electrospun carbon fiber as a magnetic heterogeneous catalyst for activating peroxymonosulfate, Chemosphere, 208 (2018) 502-511.

[20] D.D. Tuan, W.D. Oh, F. Ghanbari, G. Lisak, S. Tong, K.-Y. Andrew Lin, Coordination polymer-derived cobalt-embedded and N/S-doped carbon nanosheet with a hexagonal core-shell nanostructure as an efficient catalyst for activation of oxone in water, Journal of Colloid and Interface Science, 579 (2020) 109-118.

[21] W.-C. Yun, K.-Y.A. Lin, W.-C. Tong, Y.-F. Lin, Y. Du, Enhanced degradation of paracetamol in water using sulfate radical-based advanced oxidation processes catalyzed by 3-dimensional Co3O4 nanoflower, Chemical Engineering Journal, 373 (2019) 1329-1337.

[22] Y. Sun, C. Liu, D.C. Grauer, J. Yano, J.R. Long, P. Yang, C.J. Chang, Electrodeposited Cobalt-Sulfide Catalyst for Electrochemical and Photoelectrochemical Hydrogen Generation from Water, Journal of the American Chemical Society, 135 (2013) 17699-17702.

[23] W. Li, S. Li, Y. Tang, X. Yang, W. Zhang, X. Zhang, H. Chai, Y. Huang, Highly efficient activation of peroxymonosulfate by cobalt sulfide hollow nanospheres for fast ciprofloxacin degradation, Journal of Hazardous Materials, 389 (2020) 121856.

[24] J.-Y. Yin, E. Kwon, B.X. Thanh, G. Lisak, W.D. Oh, K.-Y.A. Lin, Cobalt sulfide nanosheets derived from sulfurization of Prussian blue analogue as an enhanced catalyst for activating monopersulfate to degrade caffeine, Journal of the Taiwan Institute of Chemical Engineers, 123 (2021) 115-123.

[25] J.-Y. Yin, W.D. Oh, E. Kwon, B.X. Thanh, S. You, H. Wang, K.-Y.A. Lin, Cobalt sulfide nanofilm-assembled cube as an efficient catalyst for activating monopersulfate to degrade UV filter, 4,4′ -dihydroxybenzophenone, in water, Colloids and Surfaces A: Physicochemical and Engineering Aspects, 625 (2021) 126891.

[26] L.-L. Feng, M. Fan, Y. Wu, Y. Liu, G.-D. Li, H. Chen, W. Chen, D. Wang, X. Zou, Metallic Co_9S_8 nanosheets grown on carbon cloth as efficient binder-free electrocatalysts for the hydrogen evolution reaction in neutral media, Journal of Materials Chemistry A, 4 (2016) 6860-6867.

[27] L. Sun, Y. Bai, K. Sun, Organic molecule controlled synthesis of three-dimensional rhododendron-like cobalt sulfide hierarchitectures as counter electrodes for dye-sensitized solar cells, RSC Advances, 4 (2014) 42087-42091.

[28] J. Zhu, L. Xiang, D. Xi, Y. Zhou, J. Yang, One-step hydrothermal synthesis of flower-like CoS hierarchitectures for application in supercapacitors, Bulletin of Materials Science, 41 (2018) 54.

[29] K. Qin, L. Wang, S. Wen, L. Diao, P. Liu, J. Li, L. Ma, C. Shi, C. Zhong, W. Hu, E. Liu, N. Zhao, Designed synthesis of NiCo-LDH and derived sulfide on heteroatom-doped edge-enriched 3D rivet graphene films for high-performance asymmetric supercapacitor and efficient OER, Journal of Materials Chemistry A, 6 (2018) 8109-8119.

[30] C.A. Martínez-Huitle, E. Brillas, Decontamination of wastewaters containing synthetic organic dyes by electrochemical methods: A general review, Appl Catal B, 87 (2009) 105-145.

[31] C. Lops, A. Ancona, K. Di Cesare, B. Dumontel, N. Garino, G. Canavese, S. Hérnandez, V. Cauda, Sonophotocatalytic degradation mechanisms of Rhodamine B dye via radicals generation by micro- and nano-particles of ZnO, Applied Catalysis B: Environmental, 243 (2019) 629-640.

[32] M. Hu, X. Yan, X. Hu, R. Feng, M. Zhou, High-capacity adsorption of benzotriazole from aqueous solution by calcined Zn-Al layered double hydroxides, Colloids and Surfaces A: Physicochemical and Engineering Aspects, 540 (2018) 207-214.

[33] R. Guo, L.-c. Nengzi, Y. Chen, Y. Li, X. Zhang, X. Cheng, Efficient degradation of sulfamethoxazole by CuCo LDH and LDH@fibers composite membrane activating peroxymonosulfate, Chemical Engineering Journal, 398 (2020) 125676.

[34] L. Jin, L. Cai, D. Chen, W. Wang, H. Shen, F. Zhang, Efficient silicon solar cells applying cuprous sulfide as hole-selective contact, Journal of Materials Science, 54 (2019) 12650-12658.

[35] Y. Pan, Y. Fang, H. Jin, M. Zhang, L. Wang, S. Ma, H. Zhu, M. Du, A Highly Active and Robust CoP/CoS_2-Based Electrocatalyst Toward Overall Water Splitting, Electrocatalysis, 10 (2019) 253-261.

[36] W. Liu, C. Lu, X. Wang, K. Liang, B.K. Tay, In situ fabrication of three-dimensional, ultrathin graphite/carbon nanotube/NiO composite as binder-free electrode for high-performance energy storage, Journal of Materials Chemistry A, 3 (2015) 624-633.

[37] Q. Wang, Y. Shao, N. Gao, W. Chu, J. Chen, X. Lu, Y. Zhu, N. An, Activation of peroxymonosulfate by Al_2O_3-based $CoFe_2O_4$ for the degradation of sulfachloropyridazine sodium: Kinetics and mechanism, Separation and Purification Technology, 189 (2017) 176-185.

[38] A. Rastogi, S.R. Al-Abed, D.D. Dionysiou, Sulfate radical-based ferrous–peroxymonosulfate oxidative system for PCBs degradation in aqueous and sediment systems, Applied Catalysis B: Environmental, 85 (2009) 171-179.

[39] W. Guo, S. Su, C. Yi, Z. Ma, Degradation of antibiotics amoxicillin by Co_3O_4-catalyzed peroxymonosulfate system, Environmental Progress & Sustainable Energy, 32 (2013) 193-197.

[40] M.R. Islam, M.G. Mostafa, Characterization of textile dyeing effluent and its treatment using polyaluminum chloride, Applied Water Science, 10 (2020) 119.

[41] D.A. Yaseen, M. Scholz, Textile dye wastewater characteristics and constituents of synthetic effluents: a critical review, International Journal of Environmental Science and Technology, 16 (2019) 1193-1226.

[42] F. Qi, W. Chu, B.B. Xu, Modeling the heterogeneous peroxymonosulfate/Co-MCM41 process for the degradation of caffeine and the study of influence of cobalt sources, Chem Eng J, 235 (2014) 10-18.

[43] L.J. Xu, W. Chu, L. Gan, Environmental application of graphene-based $CoFe_2O_4$ as an activator of peroxymonosulfate for the degradation of a plasticizer, Chemical Engineering Journal, 263 (2015) 435-443.

[44] P. Liang, C. Zhang, X. Duan, H. Sun, S. Liu, M.O. Tade, S. Wang, An insight into metal organic framework derived N-doped graphene for the oxidative degradation of persistent contaminants: formation mechanism and generation of singlet oxygen from peroxymonosulfate, Environmental Science: Nano, 4 (2017) 315-324.

[45] R. Luo, M. Li, C. Wang, M. Zhang, M.A. Nasir Khan, X. Sun, J. Shen, W. Han, L. Wang, J. Li, Singlet oxygen-dominated non-radical oxidation process for efficient degradation of bisphenol A under high salinity condition, Water Research, 148 (2019) 416-424.

[46] S. Yang, P. Wu, J. Liu, M. Chen, Z. Ahmed, N. Zhu, Efficient removal of bisphenol A by superoxide radical and singlet oxygen generated from peroxymonosulfate activated with Fe0-montmorillonite, Chemical Engineering Journal, 350 (2018) 484-495.

[47] L. Peng, X. Gong, X. Wang, Z. Yang, Y. Liu, In situ growth of ZIF-67 on a nickel foam as a three-dimensional heterogeneous catalyst for peroxymonosulfate activation, RSC Advances, 8 (2018) 26377-26382.

[48] R. Lan, W. Su, J. Li, Preparation and Catalytic Performance of Expanded Graphite for Oxidation of Organic Pollutant, Catalysts, 9 (2019) 280.

[49] X. Duan, K. O'Donnell, H. Sun, Y. Wang, S. Wang, Sulfur and Nitrogen Co-Doped Graphene for Metal-Free Catalytic Oxidation Reactions, Small, 11 (2015) 3036-3044.

[50] R. Hailili, C. Wang, E. Lichtfouse, Perovskite nanostructures assembled in molten salt based on halogen anions KX (X = F, Cl and Br): Regulated morphology and defect-mediated photocatalytic activity, Applied Catalysis B: Environmental, 232 (2018) 531-543.

[51] D. Zhang, Y. Li, J. Guo, L. Zhou, Y. Lan, C. Chen, MOFs-derived magnetic C@Cu–Ni bimetal particles: An efficient peroxymonosulfate activator for 2,4,6-trichlorophenol degradation, Chemosphere, 269 (2021) 129394.

[52] D.E. Latch, K. McNeill, Microheterogeneity of singlet oxygen distributions in irradiated humic acid solutions, Science, 311 (2006) 1743-1747.